Effect of CO$_2$ sequestration on multi-phase fluid transport and gas production in shale nanopore

Chenhao Sun[1]*, Jun Li[1], Jiawei Li[2], Sailiang Dong[1]

1 State Key Laboratory of Petroleum Resources and Prospecting, China University of Petroleum, Beijing 102249, PR China

2 Daqing Oilfield Co., Ltd. Exploration and Development Institute, 163712

(Corresponding author at China University of Petroleum (Beijing): chenhao.sun@cup.edu.cn(C. Sun))

ABSTRACT

CO$_2$ injection into shale and coalbed reservoirs to enhance methane (CH$_4$) production is treated as a better way to promote gas recovery efficien cy as well as easing carbon emission by CO$_2$ sequestration. Most CH$_4$ is adsorbed inside the organic micropores and mesopores ($\leq$ 50 nm), enjoying large surface areas and serving abundant adsorption sites. And another key structure factor is the slit, which is usually treated as a sequestration medium. To better understand the microscopic mechanism of enhanced CH$_4$ recovery by CO$_2$ in nanopores and slit becomes necessary. Thus, Molecular Dynamics (MD) supports a solid foundation for constructing the nanosized kerogen frameworks to investigate the gas adsorption behavior on the kerogen-accessible surface. This study innovatively introduced a new method of constructing kerogen slit nanopores, making the model more practical and approaching real underground environments. The grand canonical Monte Carlo (GCMC) method is employed to uncover the gas adsorption and sequestration practices within the kerogen nanopores and slit at various subsurface conditions. According to our results, the previously overlooked slit particularly impacts gas adsorption and recovery efficiency. This study also examines the widespread water encroachments, including various pure water and saline environments. Pure moisture has an overall negative on gas adsorption and sequestration,

promoting the recovery efficiency of CH$_4$ by CO$_2$ injection. Moreover, saline has a further enhanced negative influence on gas adsorption, whereas it advantages the displacement process. Ethane (C$_2$H$_6$) influences the CH$_4$ adsorption negatively but favors the recovery process. This work shows significant importance in underlining the kerogen slit nanopores structure and develops the knowledge of the comprehensive underground conditions work on gas adsorption and recovery mechanisms at a thorough level to enhance CH$_4$ extraction and CO$_2$ utilization and sequestration.

Keywords: CO$_2$ sequestration, fluid transport, shale, molecular simulation

1. INTRODUCTION

Methane gas from unconventional reservoirs has become the most attractive green resource due to the low carbon emission, low production cost and environmental-friendly performance. CO$_2$ enhanced methane recovery technique has been applied to promote hydrogen production and ease carbon emission.[2-9] This technique is developed because of the low efficiency of the conventional adopted depressurization methods performed in shale and coalbed reservoirs, which are usually low porosity and permeability.[10-14] It has been successfully applied to

improve the gas production potential and validated in laboratory and field experiments.

Unconventional reservoirs are highly heterogeneous and anisotropic, and most adsorption processes perform in organic substances.[6,15-19] Thus, this study focuses on kerogen fragments, the primary component of organic substance, and contributes to the significant gas adsorption.[7,9,20-24] Investigations of the molecular adsorption and recovery process on kerogen at a great depth by taking comprehensive influencing factors into account for CH_4 recovery and CO_2 sequestration become significant.

According to the laboratory experiments, most are undertaken at a narrow pressure range, preliminary examinations of the coupled impacting factors due to the massive workload at various temperature and pressure points, resulting in inadequate guidelines for CH_4 production and CO_2 sequestration.[16,25,26] Whereas, Molecular Dynamics is a more feasible and time-saving method to provide comprehensive subsurface conditions, especially with multiple influencing terms, providing another aspect to reveal the microscopic mechanisms.

Previous simulation studies were generally executed solely on the matrix nanopores or merely inside the slit, losing essential characteristics of reservoir structure. Furthermore, previous conclusions are observed based on limited pressure and temperature, which are inadequate to build practical guidelines for CH_4 production. Moreover, the mechanisms of adsorption and transportation inside the nanopores and slit are different owing to the pore size deviation, of which surface area and adsorption sites vary considerably. Thence, the gas adsorption mechanisms between micropores and slit have not been investigated and revealed at a deep level.

Water encroachments widespread subsurface, as the reservoirs are connected wholly or partly with hydro-geologic faults, making it essential to reveal the water influence on gas adsorption.[3] Moreover, because of the superior affinity between H_2O and the hydrophilic functional groups from the organic fragment, the adsorption mechanisms become more complex.[8,27-30] Many studies have explored the pure water impacts,

showing an overall reduction in single-phase gas adsorption; moisture content at 1.8 wt% out of 2.4 wt% has the most negative effect on type III-A kerogen.[31,32] The excess and absolute adsorption of CH_4 perform a sharp drop with the rising moisture content up to 3 wt% on a kerogen model of middle-rank coal.[33] Below 3 wt% moisture content, continuously hinders impact on CH_4 excess adsorption, which discourages industrial production.[34] However, the moisture effect on pure and binary gas mixtures has not been studied at a great depth. On the one hand, the moisture content is generally employed below 3 wt%, which is insufficient to provide general knowledge for gas adsorption mechanisms. On the other hand, the interval scale is usually too broad to manifest the influence detailly, and the principal moisture effect has been revealed at a developed level.

Furthermore, pure water is insufficient to represent the underground water, which contains ions, making the simulation results deviate from the field measurements. Typically, Na^+ is the primary cation presenting a high concentration, and Cl^- is the basic anion owing to the depositional environment.[35-37] It has been observed that CH_4 adsorption is further reduced with the growing NaCl concentration at 5 wt% moisture content in a three-layer graphene slit.[38] Similarly, CH_4 adsorption decreases with the increasing NaCl concentration in the kerogen matrix.[34] Noticeably, the NaCl full-filled kerogen slit drops CH_4 adsorption dramatically.[39] These observations point out that the investigation on saline is indispensable.

Another influencing term is the associated gas C_2H_6, generally the second-largest deposit in unconventional reservoirs, occupying 5 wt% of the total gas components.[40] Additionally, C_2H_6 shows a high concentration in the deeper section of the reservoirs, suggesting C_2H_6 is a crucial factor. However, the effect of C_2H_6 on gas adsorption and displacement efficiency has not been addressed and understood thoroughly.

This work novelly introduces a new method of constructing a kerogen model consisting of both matrix nanopores and slit to address the differences in gas adsorption mechanisms between kerogen nanopores and slit in detail. The second innovation is that this work creatively validates the porosity of the generated model,
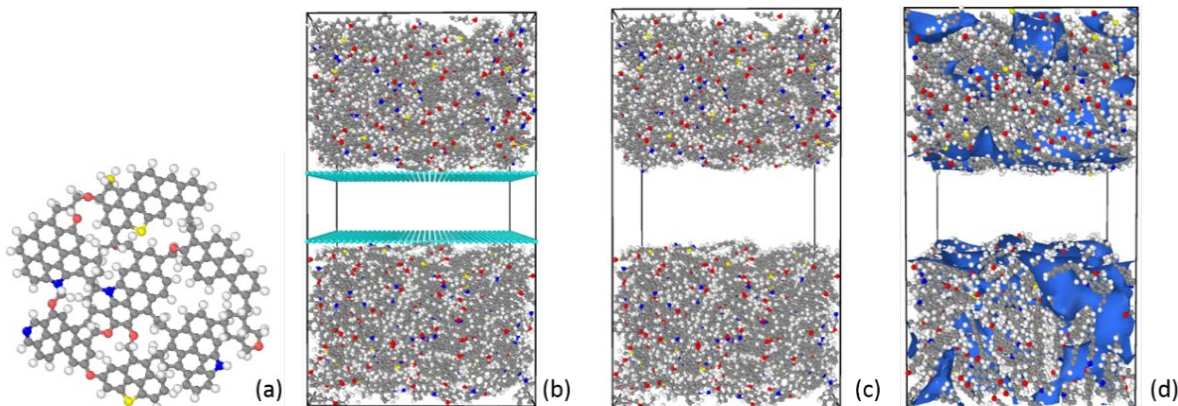
Figure 1. (a) Topology of type II-D kerogen unit; (b) The generated model with pseudo atoms; (c) final configuration by removing pseudo atoms; (d) surface mesh and pores distribution (in navy blue). Atom representation: aluminum for C, white for H, red for O, blue for N, yellow for S, and cyan for dummy atoms (visualization by Ovito[1])

which is a critical physical property in constructed model and has been overlooked in previous work. This work introduces water encroachment environments containing pure water and saline. This work examines and highlights the performance of the ions on gas adsorption and recovery processes for the first time. The pure moisture content reaches up to 5 wt% with 1 wt% increment interval. 3 mol/L to 6 mol/L of NaCl is employed to represent saline, which concentration provides sufficient ions in the simulation system to compare with the pure water. Contrasts between pure water and saline have been explored for the first time, providing a solid foundation on gas adsorption and sequestration with the presence of ions. The fourth novelty is to modify the underground environment by employing C_2H_6 with an accuracy of 0.5 wt% up to 5 wt%. Moreover, this work determines the preferential selectivity in the CH_4 and CO_2 binary mixture in the kerogen slit nanopores for the first time. Based on the previous investigation, this work improves the current understanding of enhanced CH_4 exploitation, displacement efficiency and CO_2 sequestration.

2. METHODOLOGY

2.1 Molecular Models

Simulation and experimental studies are usually established on organic matters, owing to the higher contribution to gas adsorption in unconventional reservoirs.[12,41-47] An experiment observed that the organic matter holds 200 times CH_4 than pure Kaolinite and 40 times than Illite, illustrating that organic matter holds a strong gas capacity and charges the primary adsorption process.[48] According to the previous studies, most investigations focus on the gas adsorption behavior merely in the kerogen nanopores or solely inside the slit; insufficient ones combine these two essential structures jointly. Therefore, this work takes 54 type II_D kerogen units of $C_{175}H_{102}N_4O_9S_2$ to generate the kerogen matrix with an embedded 15 Å slit to investigate the gas adoption and recovery processes between CH_4 and CO_2 with the impacting terms.[20,21] The topology of the type II_D kerogen fragment is shown in Figure 1(a) (visualization by Ovito[1]).

CH_4 and C_2H_6 are described using the OPLS All-Atom force field, allowing more flexibility for the charges and torsional energetics distribution, matching the laboratory measurements well.[49,50] CO_2 is depicted by the elementary physical model (EPM2), which employs the rigid bonds and the harmonic bond angle potential, displaying high fitting to the laboratory measurements.[51,52] The extended simple point charge (SPC/E) model describes the effectively fixed pair potentials composed of non-bonded and electronic terms for H_2O.[53] SPC/E model provides a more accurate description of H_2O above 300 K and shows high computational efficiency.[54,55] NaCl is described by the CLAYFF force field.[56-58] The detailed force field information and validation of CH_4, CO_2, C_2H_6, H_2O and NaCl are presented elsewhere.[30]

3

2.2 Simulation Details

The Molecular Dynamics (MD) grand canonical Monte Carlo (GCMC) simulations are employed and carried out in the Large-scale Atomic/Molecular Massively Parallel Simulator (LAMMPS).[59] MD method is used to obtain the optimized geometry of the adsorbent at the lowest energy and the most stable status. GCMC is applied to mimic the gas adsorption performances.

DREIDING force field exhibits superior characteristics computing energy changes during the geometry optimization process for organic matter, additionally performs favorable properties in predicting adsorption isotherm.[20,46,60-62] Thus, it is undertaken to depict the atomic interactions, Lennard Jones 12-6 potential is utilized to describe van der Waals force defining the atomic dispersion and repulsion forces between kerogen and other components (light hydrocarbons, H_2O, NaCl). Moreover, the Coulombic term is employed to determine the electrostatic potential, expressed as follows:

$$E_{potential} = E_{bonds} + E_{angles} + E_{dihedrals} + E_{impropers} + E_{crossterms} + E_{vwD} + E_{Coulombic} \quad (1)$$

where the first 5 terms represent the potential energy consisting of bonding, angle, dihedral, improper and cross energies. The last 2 factors are nonbonding terms, including the van der Waals and the electrostatic potentials.[62]

The periodic boundary condition is applied in 3D axes to avoid unfavorable atoms and interactions missing. The particle–particle and particle–mesh (PPPM) solver is employed to solve the electrostatic interactions by mapping atoms charge to a 3D mesh solving Poisson's equation on the mesh before the electric fields on the mesh point back to the traces. Verlet method is used to determine the velocity and position of each particle by calculating Newton's equation of motion.[20]

To generate the kerogen matrix with an embedded slit, kerogen units are put into one cuboid box after relaxing the single unit. Dummy atoms are then created at a particular height in the simulation box to control the position and size of the slit. The Isothermal–isobaric ensemble (NPT) is carried out from 1000 K, decreasing gradually until 338 K with the growing pressure from 0.1 MPa to 30 MPa. Each NPT run is set at 200 ps to reach equilibrium and obtain the optimum structure. Afterward, the Canonical ensemble (NVT) is taken place for 2 ns at 338 K to get the stabilized density and configuration of the model, as shown in Figure 1(b). Eventually, the dummy atoms are removed from the system to obtain the final structure for the following simulation processes, seen in Figure 1(c).

The gas adsorption and recovery processes are carried out in the grand canonical ensemble (μVT) by adopting the GCMC method with four types of particles' movement, namely insertion or deletion, transition and rotation. These actions can be accepted or rejected according to the energy produced by the geometry optimization of the trial geometry for the given engine, and accept steps merely take place with an energy reduction. The GCMC process is set at 15 million moves. The previous 14 million actions are used to obtain the equilibrium state, and the eventual 1 million steps are employed for data collection and analyses.

2.3 Validation of the generated model

One of the innovations in this work is defining the porosity of the generated model, which is employed to compare with the experimental measurements, as a critical factor in determining the established model's rationality. Thereby, the first step is to probe the density and porosity. The density is 1.23 g/cm³, falling in the range of type II kerogen density (1.18–1.35 g/cm³).[63-65] The constructed surface mesh and pores distribution is computed as 22.89% by inserting Helium atoms by Ovito, as seen in Figure 1(d). The porosity computed by PoreBlazer v4.0 software is 22.21%, suggesting a slight deviation compared to the 23.09% probed by Helium in this work, and 22.89% investigated by Ovito. PoreBlazer v4.0 software is also used to obtain the Individual and Cumulative Pore Size Distribution.[66] Additionally, the detailed physical properties of the generated model are listed in Table S2. The probed porosity in this work is identical to the experimental result, 21% for a typical brown coal char, similar to the coal samples from Queensland and NSW.[64,65,67] And additionally agrees with the Barnett shale samples (20%-25%), and Ho's observation of 26%.[68,69] This initial validation of the constructed kerogen model is consistent with the

natural shale and coal samples.

The next validation step is based on the excess adsorption, converted from the absolute adsorption and used to contrast with the experimental outcomes. As seen in Figure 2, the excess adsorption of this study is in the black-filled circles, which matches well with the experimental measurements and the simulation outcomes.[17,34,70] The simulation results from this work are in the middle of the previous studies, implying that the determined magnitude is reasonable. The preceding discussions make the generated model reliable and can be utilized for further simulation.
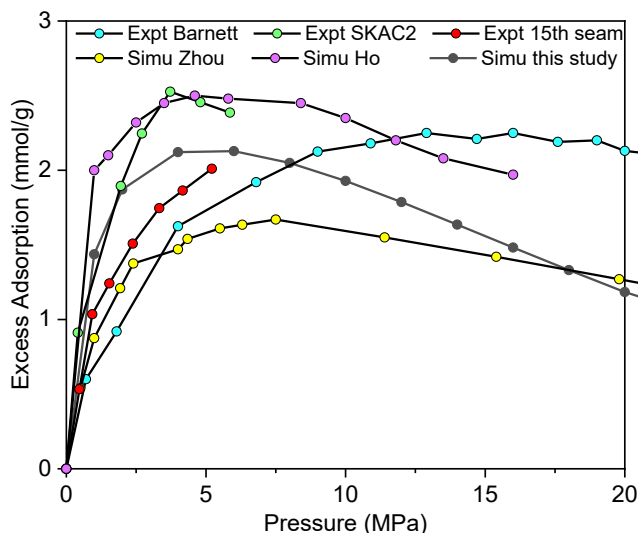

Figure 2. CH$_4$ excess adsorption of experimental and simulation measurements compared to this work.

3. RESULTS AND DISCUSSION

3.1 Single Component Adsorption

3.1.1 Gas Adsorption and Comparisons between the Kerogen Nanopores and Slit

This section discusses and compares the absolute and excess adsorptions, conducted and determined on the kerogen nanopores and slit from 308 K to 368 K. This part highlights the primary differences in adsorption mechanisms between the nanopores and slit to manifest the motive of the model generation.

Adsorption isotherm is a criterion for characterizing gas adsorption capacity. GCMC simulation gives the absolute adsorption, the sum of the bulk phase adsorbates and the excess adsorption. Absolute adsorption parameters of pure CH$_4$ and CO$_2$ are determined by the Langmuir model (Equation 2),[71]

$$n^{abs} = n^{max}(T)\frac{b(T)*p}{1+b(T)*p} \tag{2}$$

where n^{abs} stands for the absolute adsorption amount (mmol/g), n^{max} is the Langmuir maximum adsorption amount (mmol/g), p is the pressure (MPa), and b represents the Langmuir coefficient (MPa^{-1}) or the adsorption rate.[71]

Figures 3(a) and (b) describe the absolute adsorption of CH$_4$ and CO$_2$ on the kerogen nanopores. Figures 3(c) and (d) illustrate the absolute adsorption on the whole model (including kerogen nanopores and slit). Figures 3(e) and (f) represent the adsorption deviations between the kerogen nanopores and the whole model for CH$_4$ and CO$_2$.
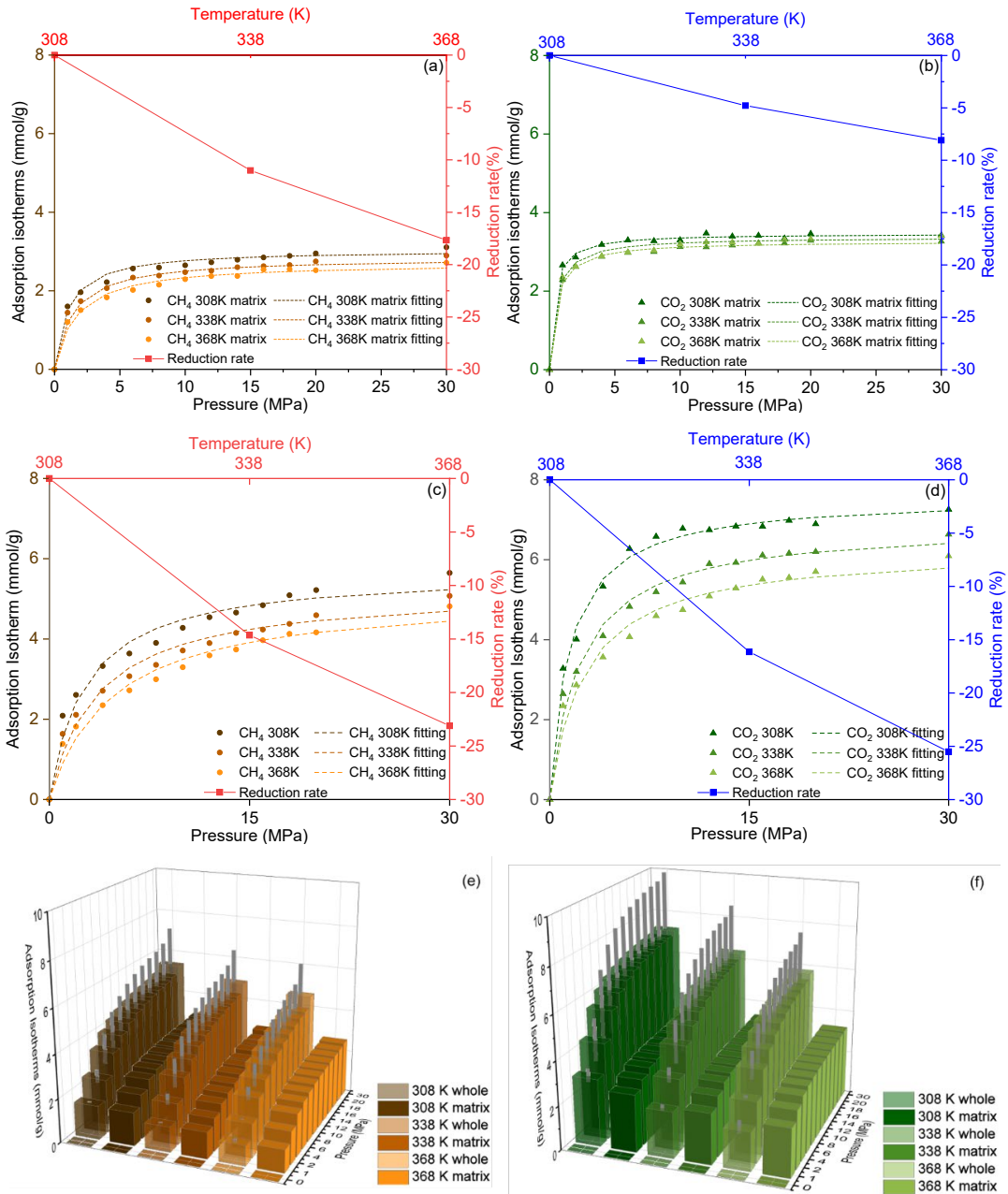
Figure 3. (a) CH_4, and (b) CO_2 adsorption on the kerogen nanopores and the Langmuir fitting; (c) CH_4, and (d) CO_2 adsorption on the whole model and the Langmuir fitting; Adsorption Deviation between the kerogen nanopores and the whole model of (e) CH_4, and (f) CO_2 at 308 K, 338 K, and 368 K

Figure 3(a) presents the CH_4 adsorption on the kerogen nanopores, identical to the previous observations of a $C_{251}H_{385}O_{13}N_7S_3$ organic matrix and a low coalification sample.[7,9] Figures 3(c) and (d) demonstrate the adsorption isotherms of CH_4 and CO_2 on the whole model, consisting of Huang's and Sui's observations.[31,72] From Figure 3, the temperature-induced uptake deviations on the kerogen nanopores are not evident compared to the whole model, suggesting

that the slit serves as a critical factor in characterizing gas storage and sequestration. The error bars of Figures 3(e) and (f) suggest that the adsorption varies apparently between the kerogen nanopores and the whole model, owing to the slit. A detailed discussion of the absolute adsorption differences based on the influences of temperature and pressure is presented below.

Temperature-induced adsorption variations between kerogen nanopores and the whole model are

discussed. Both CH_4 and CO_2 show a more evident adsorption shrink on the whole model than kerogen nanopores with the increasing temperature, suggesting that temperature impacts more with the presence of the slit. This scenario is because the slit has less surface area and adsorption sites, leading to a weaker interaction with the gas molecules. Additionally, owing to the less overlapping effect of the slit, the growing temperature promotes the particles' kinetic energy and facilitates gas molecules to escape the energy barrier and become free. Furthermore, the slit provides expanse space for gas molecules to travel, promoting gas molecules' collisions and the Brownian motion. Consequently, the settling time for gas molecules to attach to adsorption sites belonging to the slit surface reduces, resulting in a more apparent absolute uptake reduction with the temperature. Noteworthy, increasing temperature induces a deduction of 10% for CH_4 and 7% for CO_2 on the kerogen nanopores, compared to 23% for CH_4 and 25% for CO_2 on the whole model. This enhanced reduction is owing to the slit, revealing the gas capacity of which is

adsorption performance than CH_4, suggesting that the organic matter holds a significantly high CO_2 adsorption capacity. CO_2 has a higher adsorption rate than CH_4, showing the superior affinity between CO_2 and the organic substances, implying CO_2 could capture adsorption sites faster than CH_4.

Pressure-induced adsorption variations between kerogen and the whole model are discussed below. The adsorption deviations become evident with the growing pressure, and kerogen nanopores performs an earlier turning point than the whole model. It is attributed to the strong overlapping effect that induces robust interaction with the gas particles, leading to the adsorption sites being majority occupied at low pressure. Two candidates are almost saturated at 6 MPa, and the growing pressure becomes a minor influence factor in the adsorption process. It also indicates a dynamic equilibrium between the pressure-induced enhanced absolute adsorption and the mechanical compression at 6 MPa.

On the other hand, the turning points are postponed

Table 1. Langmuir fitting Parameters for CH_4 and CO_2 at 308 K, 338 K and 368K respectively on kerogen nanopores and the whole model.

CH_4	n^{max} (mmol/g)	b (MPa^{-1})	R^2	CO_2	n^{max} (mmol/g)	b (MPa^{-1})	R^2
matrix				matrix			
308 K	3.045	0.983	0.9809	308 K	3.464	2.966	0.9964
338 K	2.919	0.8236	0.9853	338 K	3.376	2.11	0.9966
368 K	2.719	0.6046	0.9856	368 K	3.27	2.021	0.9927
whole model				whole model			
308 K	5.7	0.3696	0.9701	308 K	7.588	0.6667	0.9933
338 K	5.256	0.25	0.9733	338 K	6.898	0.436	0.9873
368 K	5.142	0.1824	0.9718	368 K	6.293	0.2757	0.9785

more temperature-dependence.

Table 1 displays the Langmuir fitting parameters for CH_4 and CO_2. The Langmuir maximum adsorption reduces with the temperature, in line with the adsorption isotherms in Figure 3. Another observation is that the kerogen has a much higher adsorption rate than the whole model, especially at high temperatures. This scenario is because the slit has a less overlapping effect, which weakens the interaction strength with the gas molecules. Column n^{max} indicates that CO_2 has superior

for the whole model because the slit weakens the interaction with gas molecules. In addition, the increasing pressure restricts the particles' free movement and gas diffusion within the slit space. Furthermore, the growing pressure induces mechanical compression, which increases the bulk phase density, especially in the slit, enhancing the absolute adsorption. Thus, the absolute adsorption expands with the increasing pressure in the whole model.

The excess adsorption and comparison between CH_4 and CO_2 on the kerogen nanopores and the whole model are analyzed. The excess amount can be determined by subtracting the fluid occupying the pore volume at bulk phase density from the absolute uptakes. The relationship between the excess amount and the total adsorption is shown in Equation (3):

$$n^{ex} = n^{abs} - \rho_{bulk}V_{pore} \tag{3}$$

where ρ_{bulk} is the fluid's density in the bulk phase, V_{pore} is the pore volume.

CH_4 excess adsorption in this work is 2.97 mmol/g at 3 MPa and 338 K, agreeing with the experimental measurement, 2.997 mmol/g at 2.98 MPa.[73] The
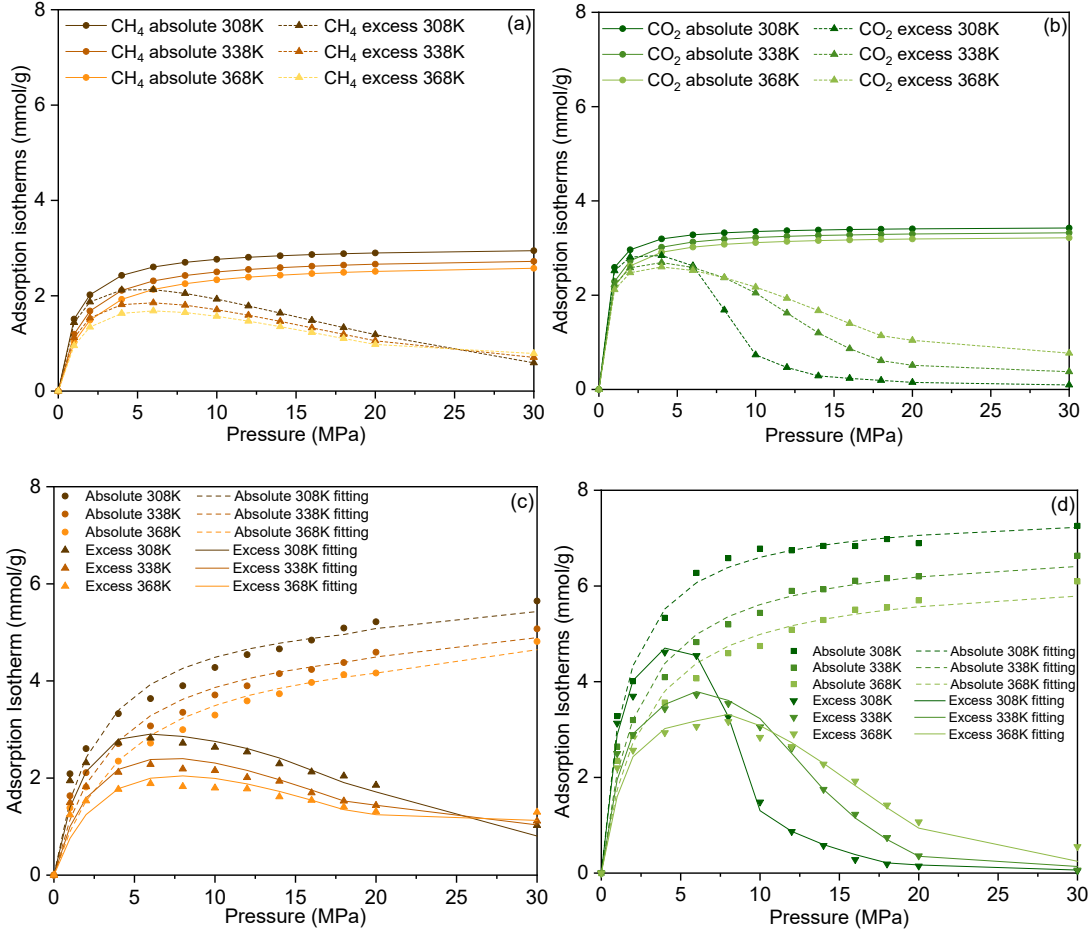

Figure 4. (a) CH_4, and (b) CO_2 absolute and excess adsorption isotherms on kerogen nanopores; (c) CH_4, and (d) CO_2 on the whole model and the Langmuir fitting at 308 K, 338 K and 368 K

Figure 4(a) performs the CH_4 excess adsorption intersection is approximately 24 MPa under three temperatures, suggesting low temperature favors the excess adsorption below 24 MPa, and high temperature encourages the excess adsorption above 24 MPa on kerogen nanopores. CH_4 peaks at 6 MPa, indicating the pressure-induced enhanced absolute adsorption is the principal effect below 6 MPa. Whereas, CH_4 excess adsorption shrinks above 6 MPa, revealing that the pressure-induced mechanical compression is the dominant performance. Above 24 MPa, at 368 K, the

negligible difference indicates the accuracy of this work. excess isotherm is almost parallel to the x-axis, showing a dynamic equilibrium between the enhanced absolute adsorption and the mechanical compression, suggesting pressure becomes a negligible impact factor. CH_4 excess adsorption in the whole model presents a similar trend to the kerogen. However, Figure 4(c) illustrates a delicate higher shape under the same condition compared to Figure 4(a), owing to the slit influence.

Figure 4(b) presents two intersections of CO_2 excess adsorption isotherms on kerogen. Furthermore, the high temperature favors the excess adsorption process until the second intersection at 9 MPa, and an earlier intersection pressure than CH_4. Additionally, the increasing temperature postpones the peak excess adsorption, shifting to high pressure. Like CH_4, CO_2 peak excess adsorption on the whole model is delayed than the kerogen. Moreover, the deviation in the excess adsorption isotherms is more evident at low pressure on the whole model, indicating the slit significantly influences CO_2 excess adsorption and sequestration.

According to the previous discussion, it is crucial to consider the slit effect on the gas adsorption, owing to the deviations in adsorption characteristics and capacity. Thence, the generated model in this work is critical. From the computed outcomes, the peak excess adsorption of CH_4 and CO_2 perform at low pressure, suggesting that shallow reservoirs are more profitable for CH_4 exploitation and CO_2 sequestration.

Isosteric heat of adsorption and standard entropy are crucial factors defining adsorption characteristics.[31,33,74] In terms of further validating the generated model and simulation outcomes, Equation (4) is engaged for determining the relationship between the isosteric heat of adsorption q (kJ/mol) and the standard entropy of adsorption ΔS^0 (kJ/mol·K^{-1}),

$$1/b_L = \exp (q/RT + \Delta S^0/R) \qquad (4)$$

where R is the gas constant, and values for b_L are from in Table 2.

Figure 5 performs the correlation between the natural logarithm of the Langmuir pressure reciprocal and the temperature reciprocal for CH_4 and CO_2 on the whole model utilizing the Langmuir data at 308 K, 338 K and 368 K from Table 2. The trendline correlation coefficient R^2 is 0.9999 out of 1 for the scatters, showing high exact simulation outcomes of this work. The isosteric adsorption heat of CH_4 is computed as 11.1 kJ/mol, which is in the range of the experimental measurements 10.3-21.9 kJ/mol.[75] And the intersection

with the x-axis is the standard entropy of adsorption as -44.8 kJ/mol·K^{-1}, falling in the laboratory range (-42 to -74.7 kJ/mol·K^{-1}).[76] The adsorption heat and standard entropy of adsorption for CO_2 are 13.8 kJ/mol and -48.1 kJ/mol·K^{-1} with a R^2 of 0.9947. The measurements exhibit that CO_2 has a higher adsorption heat over CH_4, manifesting that CO_2 liberates more energy during the
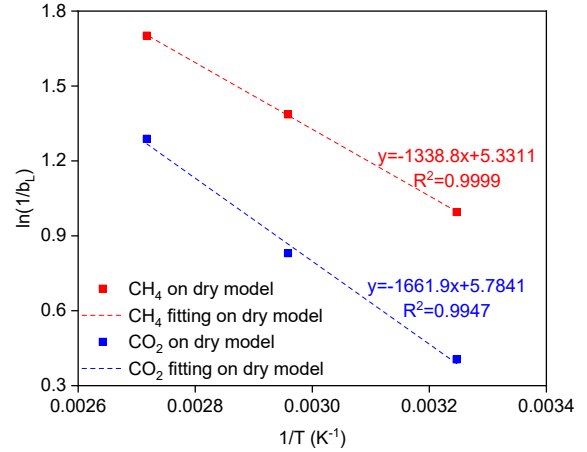

Figure 5. Isosteric heat of adsorption and the standard entropy of CH_4 and CO_2 on the whole model.

adsorption and performs a more vital interaction with the model.

3.1.2 Gas Adsorption on the whole model under Water-Encroachment conditions

The validation, rationality, and necessity of the generated model including nanopores and slit are discussed in previous sections. This part will examine the moisture effect on CH_4 adsorption, conducted on the whole model. The moisture content depends on the number of H_2O molecules, quantifying based on the Equation (5):

$$\varpi = \frac{N_{H2O}*M_{H2O}}{N_{H2O}*M_{H2O}+M_{matrix}} \qquad (5)$$

where N_{H2O} is the number of water molecules, M_{H2O} is the water molar weight (g/mol), M_{matrix} is the molar weight of the whole model(g/mol), and ϖ is the moisture content (wt%) specified in this work.
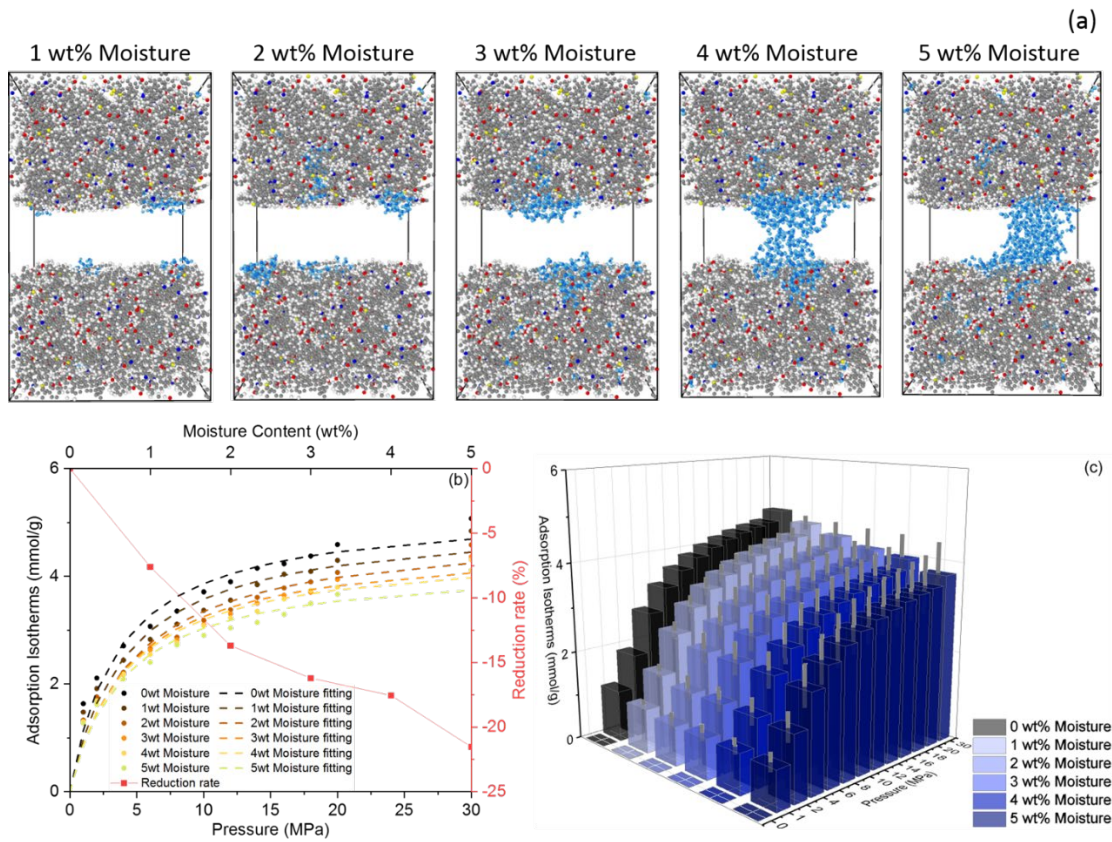
Figure 6. (a) H_2O molecular distribution at 1 wt% to 5 wt% moisture content; (b) CH_4 adsorption and Langmuir fitting vs reduction rate; (c) Deviations in the CH_4 adsorption with error bars under various moisture contents.

According to the 1-5 wt% moisture content, the H_2O molecules are computed as 77 (0.58 mmol/g), 148 (1.11 mmol/g), 227 (1.71 mmol/g), 309 (2.32 mmol/g), and 379 (2.85 mmol/g), which molecular distributions are displayed in Figure 6(a). Figure 6(b) shows the CH_4 adsorption isotherms from 0 wt% to 5 wt% moisture content. Figure 6(c) provides the CH_4 adsorption isotherms with error bars compared with the dry model, following the reduction order: 7.6%, 13.7%, 16.2%, 17.5%, and 21.5%. The reduction rate is gradually weakened until 4 wt% before a pronounced decline at 5 wt% moisture content, resulting from the H_2O molecular distribution. Below 2 wt%, the dispersed H_2O molecules spread along and occupy the adsorption sites of the slit surface, see in Figure 6(a), leaving CH_4 a challenging adsorption environment, presenting an evident reduction rate in Figure 6(b). At 3 wt% moisture content, H_2O molecules aggregate on the slit surface and occupy the adsorption sites of the kerogen nanopores, making

the previously H_2O occupied adsorption sites vacant for CH_4 to capture, easing the CH_4 reduction rate. At 4 wt% moisture content, the rising H_2O molecules accumulate into larger water clusters and occupy the slit space. The accumulation formed secondary adsorption sites and space mitigate the negative influence of H_2O molecules, and a gentle CH_4 reduction performs. However, at 5 wt%, due to the high-water density (2.85 mmol/g), H_2O molecules capture more adsorption sites of the slit surface, kerogen nanopores, and the slit space. It makes the environment unfavorable for CH_4 and results in a severe reduction in CH_4 adsorption. The slit presents a considerable impact on H_2O distribution and CH_4 adsorption, indicating its indispensable feature in reservoirs.

Table 2. Langmuir fitting Parameters for CH_4 at 0 wt% - 5 wt% moisture content.

CH_4	n^{max} (mmol/g)	b (MPa^{-1})	R^2
0 wt% Moisture Content	5.256	0.25	0.9733
1 wt% Moisture Content	5.066	0.2404	0.9694
2 wt% Moisture Content	4.903	0.2307	0.9721
3 wt% Moisture Content	4.639	0.2349	0.9762
4 wt% Moisture Content	4.523	0.2383	0.9736
5 wt% Moisture Content	4.239	0.2304	0.9684

Table 2 displays the Langmuir fitting parameter information for CH_4, implying that the moisture impedes the CH_4 Langmuir maximum adsorption and interaction rate.

The following section is based on the previous scenario of 5 wt% moisture content, of which NaCl is introduced to explore the salinity impact on gas adsorption. The introduced ions are computed based on the H_2O molecules, 20, 27, 34 and 42 pairs corresponding to 3 mol/L to 6 mol/L NaCl concentration.

Figure 7(a) depicts that the rising NaCl concentration negatively impacts CH_4 adsorption, suggesting ions perform an enhanced reduction effect.
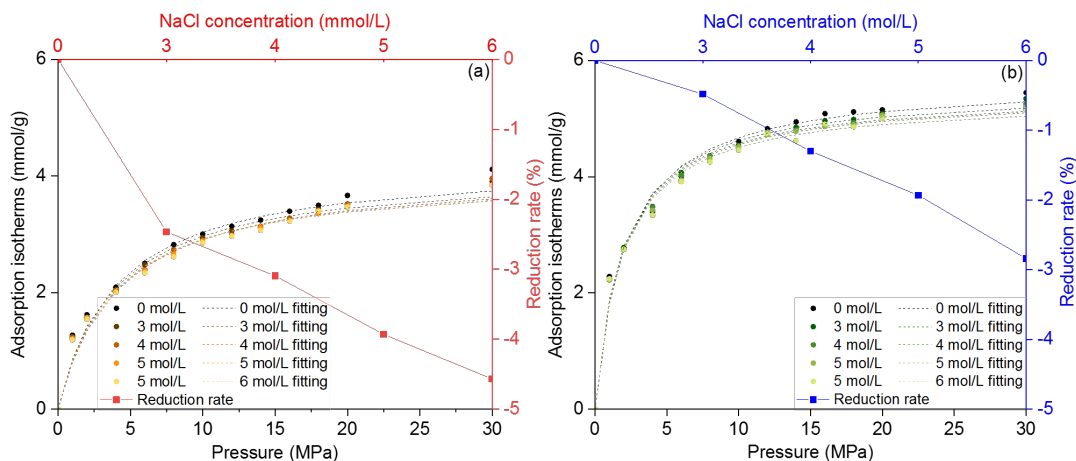
ions narrow the CH_4 solubility. On the other hand, ions ease the CH_4 adsorption due to neither dipole nor quadrupole moment nature of CH_4, leading to the reduction being almost linear with the gradual increase in NaCl concentration. In comparison, Figure 7(b) shows a gentle CO_2 adsorption reduction with the increasing NaCl. It is because the growing salinity decreases the CO_2 solubility, but the interactions between the NaCl and CO_2 neutralize this solubility reduction. However, the enhanced interactions cannot offset the solubility decrease, leading to an overall reduction in CO_2 adsorption. Noticeably, because of the stronger interaction between ions and CO_2 over CH_4, the reduction scale of CO_2 is minor than CH_4.

Table 3 summarizes the Langmuir fitting parameters of CH_4 and CO_2, Langmuir maximum adsorption of which decrease with the NaCl concentration, showing the negative effect of ions on gas adsorption. Additionally, an enhanced reduction in saline than in pure water is observed. CH_4 adsorption rate shrinks with the growing NaCl concentration, suggesting the salinity weakens the interaction strength with CH_4. CO_2 performs an increased adsorption rate with the salinity, suggesting ions enhances the interactions with CO_2, which inverses from CH_4.

Figure 7. Adsorption and Langmuir fitting for (a) CH_4, and (b) CO_2 at 3 mol/L to 6 mol/L NaCl concentration vs reduction rate.

Two main reasons cause this scenario. On the one hand,

Table 3. Langmuir fitting Parameters for CH_4 and CO_2 under various NaCl concentrations at 5 wt% moisture content.

CH₄				CO₂			
NaCl concentration	n^{max} (mmol/g)	b (MPa⁻¹)	R^2	NaCl concentration	n^{max} (mmol/g)	b (MPa⁻¹)	R^2
0 mol/L	4.239	0.2364	0.9684	0 mol/L	5.662	0.4727	0.9876
3 mol/L	4.113	0.2298	0.9798	3 mol/L	5.512	0.5213	0.9912
4 mol/L	4.102	0.2242	0.9747	4 mol/L	5.449	0.5273	0.9926
5 mol/L	4.055	0.2173	0.9709	5 mol/L	5.429	0.5221	0.9904
6 mol/L	4.004	0.2119	0.9791	6 mol/L	5.362	0.5445	0.9892

3.1.3 Gas Adsorption on the whole model with the presence of C_2H_6

This section will discuss the CH_4 adsorption in the presence of C_2H_6 contents from 0 wt% to 5 wt% with an incremental interval of 0.5 wt%, the quantification of C_2H_6 numbers is based on Equation (5), which are 23 (0.17 mmol/g), 45 (0.34 mmol/g), 68 (0.51 mmol/g), 90 (0.68 mmol/g), 113 (0.85 mmol/g), 135 (1.01 mmol/g), 179 (1.34 mmol/g), and 222 (1.67 mmol/g) corresponding to 0.5 wt%, 1 wt%, 1.5 wt%, 2 wt%, 2.5

space with the growing C_2H_6 molecules.

As seen in the double-Y figure of Figure 8(b), CH_4 adsorption decreases with the growing C_2H_6 content, from 7.9% reduction at 0.5 wt% to 30.9% at 5 wt% C_2H_6. The decline in CH_4 adsorption depends on two reasons. As discussed before, C_2H_6 has a high affinity with the kerogen, occupying more adsorption sites, forcing CH_4 molecules to reside inside the slit and leading to a desorption process. Secondly, the dumbbell-type diatomic molecular structure of C_2H_6 has a larger kinetic
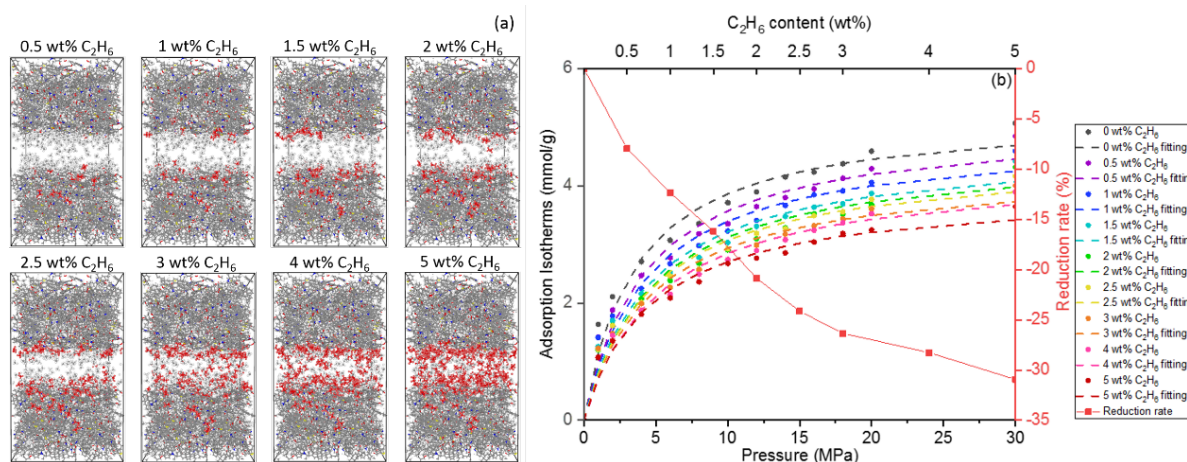

Figure 8. (a) Molecular distribution at 0.5 wt% to 5 wt% C_2H_6 contents, (b) CH_4 adsorption isotherms under various C_2H_6 contents vs reduction rate.

wt%, 3 wt%, 4 wt% and 5 wt% C_2H_6 content.

Figure 8(a) presents that C_2H_6 prefers attaching to the adsorption sites of the kerogen nanopores than the slit surface below 3 wt% C_2H_6 content. With the growing C_2H_6 content, C_2H_6 molecules gradually occupy the adsorption sites along the slit surface and inside the slit space. The adsorption sites inside the matrix nanopores and along the matrix surface are initially held by CH_4, which is gradually driven to accommodate inside the slit

diameter of 0.44 nm over CH_4 (0.38 nm), occupying a larger pore volume, leaving CH_4 in an unfavorable environment.

Noticeably, C_2H_6 hinders CH_4 adsorption more severer than H_2O. The large size of C_2H_6 occupies more pore volume and slit space than H_2O (0.26 nm). In addition, the low adhesion force and weak hydrogen bond of C_2H_6 favor the dispersed C_2H_6 molecules to spread throughout, leading to a more evident reduction scale over H_2O. The solubility of CH_4 in C_2H_6 is negligible than that of H_2O, which further drops CH_4 adsorption.

Table 4. Langmuir fitting Parameters for CH_4 under various C_2H_6 contents.

CH_4	n^{max} (mmol/g)	b (MPa^{-1})	R^2
0 wt% C_2H_6	5.256	0.25	0.9733
0.5 wt% C_2H_6	5.086	0.2361	0.9736
1 wt% C_2H_6	4.864	0. 2312	0.9718
1.5 wt% C_2H_6	4.69	0.2186	0.9732
2 wt% C_2H_6	4.612	0.2099	0.9682
2.5 wt% C_2H_6	4.513	0. 204	0.9703
3 wt% C_2H_6	4.499	0.2015	0.973
4 wt% C_2H_6	4.313	0.1942	0.9773
5 wt% C_2H_6	3.941	0.1883	0.9779

Table 4 depicts the CH_4 Langmuir maximum adsorption and the adsorption rate continue shrinking with increasing C_2H_6 content, suggesting the negative influence of C_2H_6 on the CH_4 adsorption process.

3.2 Competitive Adsorption and Preferential Selectivity $S_{CO2/CH4}$

The competitive adsorption between CH_4 and CO_2, and the preferential adsorption performance are conducted the whole model, and detailed information is analyzed in this section. Furthermore, preferential adsorption selectivity is an indicator for evaluating the more substantial potential of the adsorbent of the adsorbate over the other. This work employs this indicator to define the displacement efficiency of CH_4 by CO_2. It is calculated by Equation (6):

$$S_{CO_2/CH_4} = \frac{x_{CO_2}/x_{CH_4}}{y_{CO_2}/y_{CH_4}} \tag{6}$$

where $S_{CO2/CH4}$ stands for the preferential adsorption of CO_2 over CH_4, x_{CO2}, x_{CH4}, y_{CO2} and y_{CH4} represent the mole fractions of CO_2 and CH_4 in the adsorbed and bulk phases. If $S_{CO2/CH4}$ is higher than one, CO_2 is preferentially adsorbed. Otherwise, CH_4 holds a superior affinity in the coalbed.

Figure 9(a) illustrates the adsorption distributions of the equimolar binary mixtures of CH_4 and CO_2 under 308 K, 338 K and 368 K. Figure 9(b) displays the increasing trend of the Preferential Selectivity $S_{CO2/CH4}$ with the temperature, similar to previous studies.[61,77,78] It shows that the $S_{CO2/CH4}$ values are above one, suggesting CO_2 has a better adsorption performance than CH_4, and can be used as the replacement agent to promote the CH_4 production. Figure 9(a) illustrates that the binary adsorption of CH_4 and CO_2 decreases with the temperature, which is more evident in the slit space. With the increasing temperature, a large amount of CO_2 molecules are still firmly attached to the adsorption sites belonging to the matrix nanopores over CH_4. Furthermore, CO_2 generally seizes the adsorption sites belonging to the surface compared to CH_4 traveling inside the slit. Thus, the increased temperature favors the preferential adsorption of CO_2. Additionally, $S_{CO2/CH4}$ drops with the growing pressure. It is attributed to CO_2 getting saturated at low pressure due to its superior affinity. However, the increasing pressure encourages the interactions between the CH_4 and the kerogen. Therefore, CH_4 starts to occupy the vacant adsorption sites left by CO_2, reducing the $S_{CO2/CH4}$.
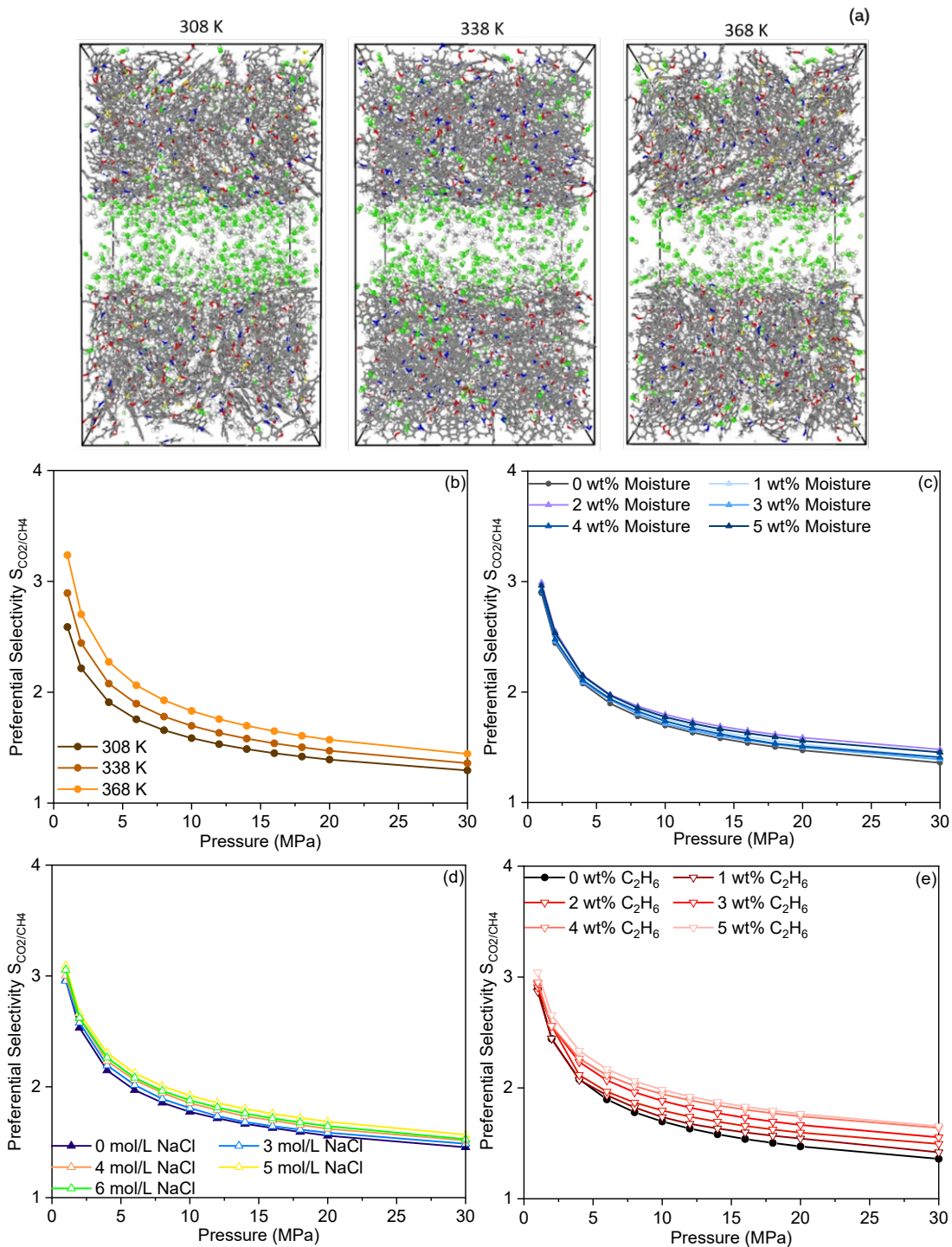
Figure 9. (a)Molecular distribution of binary mixture of CH_4 and CO_2 under various moisture contents; Preferential Selectivity $S_{CO2/CH4}$ (b) at 308 K, 338 K, and 368 K; (c) under 0 wt% to 5 wt% moisture contents; (d) under 0 mol/L to 6 mol/L NaCl.

Figure 9(c) shows the variation in $S_{CO2/CH4}$ under different moisture contents. $S_{CO2/CH4}$ are all above one, suggesting that CO_2 can be employed to promote CH_4 production in water encroached reservoirs.

Figure 9(d) presents $S_{CO2/CH4}$ variation under various NaCl concentrations. The beyond one curve implies CO_2

has an advanced interaction strength with the kerogen over CH_4, implying CO_2 can displace CH_4 in a saline environment. Increasing concentration has an overall promotion of $S_{CO2/CH4}$ compared to pure water, which is credited to the interaction between ions and CO_2 being more energetic, as mentioned in Section 3.1.3. Thus, the

14

encroached subsurface saline advantages the $S_{CO2/CH4}$, and can obtain a higher displacement efficiency.

Figure 9(e) displays $S_{CO2/CH4}$ variation under various C_2H_6 contents. All determined values are above one, showing the superior affinity of CO_2 over CH_4 with the presence of C_2H_6. Additionally, the increasing C_2H_6 content encourages $S_{CO2/CH4}$. It is attributed to CO_2 having the most affinity property with the kerogen among CH_4 and C_2H_6, the displacement process not only presences on CH_4, but CO_2 will also replace C_2H_6. The mole fraction of CO_2 in the bulk phase reduces with the growing C_2H_6 content at a pronounced scale, resulting in an overall increasing trend in $S_{CO2/CH4}$.

4. CONCLUSION

This study investigates the adsorption behavior of the pure component of CH_4 and CO_2 and their binary mixtures in realistic subsurface environments, including a wide range of temperature, pressure, water encroached scenarios, and ethane presences. And we draw the conclusions as follows,

a) This work innovatively discusses and analyzes the differences in adsorption behavior between the kerogen nanopores and slit by comparing the absolute and excess adsorption amounts. Furthermore, this work gives solid principles in highlighting the necessity of constructing of the organic model with an embedded slit, which provides a critical view of the gas adsorption and sequestration process.

b) Temperature hinders gas adsorption, high temperature provides gas molecules more energy, encouraging gas molecules to become the free state, which is more evident in slit over the kerogen nanopores. High temperature promotes the competitive adsorption between CH_4 and CO_2, advancing the preferential selectivity $S_{CO2/CH4}$.

c) Pressure promotes gas adsorption, enhancing the molecular interactions, which is more apparent in slit by showing a postponed turning point in adsorption isotherms. $S_{CO2/CH4}$ decreases with the increasing pressure. It is attributed to CO_2 almost getting saturated at low pressure, whereas CH_4 captures available vacant adsorption sites owing to the enhanced interaction strength provided by the increasing pressure.

d) Water encroachment negatively affects pure and binary gas adsorption. At low moisture content, H_2O molecules majorly occupy the adsorption sites, leaving an unfavorable adsorption environment behind. At higher moisture content, H_2O molecules further block slit space. However, it has a positive effect on $S_{CO2/CH4}$, the preloaded H_2O molecules have a more negative impact on CH_4 molecules over CO_2, leading to an overall increased trend in $S_{CO2/CH4}$. Saline shows a further hinder effect on the adsorption of the pure component, whereas an integrated promotion in $S_{CO2/CH4}$, and can promote the displacement efficiency.

e) Ethane is passive on the gas adsorption, whereas it favors the $S_{CO2/CH4}$. The preloaded C_2H_6 can be displaced by CO_2, leading to the bulk phase reduction of CO_2, resulting in $S_{CO2/CH4}$ increases.

This kerogen slit nanopores model allows us to obtain the primary information of a practical organic sample. Moreover, previous simulation outcomes have clarified the differences in the nanopores and the slit, which critically emphasizes the importance of the generated model and supplies a solid knowledge for the CO2-ECBM projects. Furthermore, based on the characteristics of the slit in the reservoir, the gas storage and sequestration potential have been detailed investigated, which would provide guidelines for CO_2 sequestration in the future.

REFERENCE

[1] Stukowski A. Visualization and analysis of atomistic simulation data with OVITO–the Open Visualization Tool. *Modelling and Simulation in Materials Science and Engineering.* 2009;18(1):015012.

[2] Zhang XG, Ranjith PG, Perera MSA, Ranathunga AS, Haque A. Gas Transportation and Enhanced Coalbed Methane Recovery Processes in Deep Coal Seams: A Review. *Energy & Fuels.* 2016;30(11):8832-8849.

[3] Karacan CÖ, Ruiz FA, Cotè M, Phipps S. Coal mine methane: A review of capture and utilization practices with benefits to mining safety and to greenhouse gas reduction. *International Journal of Coal Geology.* 2011;86(2):121-156.

[4] Lu W, Huang B, Zhao X. A review of recent research and development of the effect of hydraulic fracturing on

gas adsorption and desorption in coal seams. *Adsorption Science & Technology.* 2019;37(5-6):509-529.

[5] Arora V, Cai Y. U.S. natural gas exports and their global impacts. *Applied Energy.* 2014;120:95-103.

[6] Collell J, Galliero G, Vermorel R, et al. Transport of Multicomponent Hydrocarbon Mixtures in Shale Organic Matter by Molecular Simulations. *The Journal of Physical Chemistry C.* 2015;119(39):22587-22595.

[7] Wang T, Tian S, Li G, et al. Molecular Simulation of CO2/CH4 Competitive Adsorption on Shale Kerogen for CO2 Sequestration and Enhanced Gas Recovery. *The Journal of Physical Chemistry C.* 2018;122(30):17009-17018.

[8] Liu L, Nicholson D, Bhatia SK. Impact of H2O on CO2 Separation from Natural Gas: Comparison of Carbon Nanotubes and Disordered Carbon. *The Journal of Physical Chemistry C.* 2015;119(1):407-419.

[9] Sun H, Zhao H, Qi N, Li Y. Molecular Insights into the Enhanced Shale Gas Recovery by Carbon Dioxide in Kerogen Slit Nanopores. *The Journal of Physical Chemistry C.* 2017;121(18):10233-10241.

[10] Wang Z, Li Y, Liu H, Zeng F, Guo P, Jiang W. Study on the Adsorption, Diffusion and Permeation Selectivity of Shale Gas in Organics. *Energies.* 2017;10(1).

[11] Han W, Li A, Memon A, Ma M. Synergetic Effect of Water, Temperature, and Pressure on Methane Adsorption in Shale Gas Reservoirs. *ACS Omega.* 2021;6(3):2215-2229.

[12] Zhao H, Lai Z, Firoozabadi A. Sorption Hysteresis of Light Hydrocarbons and Carbon Dioxide in Shale and Kerogen. *Scientific Reports.* 2017;7.

[13] Wang T, Tian S, Li G, Sheng M. Selective adsorption of supercritical carbon dioxide and methane binary mixture in shale kerogen nanopores. *Journal of Natural Gas Science and Engineering.* 2018;50:181-188.

[14] Pribylov AA, Skibitskaya NA, Zekel' LA. Sorption of methane, ethane, propane, butane, carbon dioxide, and nitrogen on kerogen. *Russian Journal of Physical Chemistry A.* 2014;88(6):1028-1036.

[15] Wu T, Zhao H, Tesson S, Firoozabadi A. Absolute adsorption of light hydrocarbons and carbon dioxide in shale rock and isolated kerogen. *Fuel.* 2019;235:855-867.

[16] Tian H, Li T, Zhang T, Xiao X. Characterization of methane adsorption on overmature Lower Silurian–Upper Ordovician shales in Sichuan Basin, southwest China: Experimental results and geological implications. *International Journal of Coal Geology.* 2016;156:36-49.

[17] Ho TA, Criscenti LJ, Wang Y. Nanostructural control of methane release in kerogen and its implications to wellbore production decline. *Scientific Reports.* 2016;6(1):28053.

[18] Li P, Ma D, Zhang J, Huo Z. Wettability modification and its influence on methane adsorption/desorption: A case study in the Ordos Basin, China. *Energy Science & Engineering.* 2020;8(3):804-816.

[19] Zhang D-F, Cui Y-J, Liu B, Li S-G, Song W-L, Lin W-G. Supercritical Pure Methane and CO2 Adsorption on Various Rank Coals of China: Experiments and Modeling. *Energy & Fuels.* 2011;25(4):1891-1899.

[20] Li J, Wang Y, Chen Z, Rahman SS. Simulation of Adsorption–Desorption Behavior in Coal Seam Gas Reservoirs at the Molecular Level: A Comprehensive Review. *Energy & Fuels.* 2020;34(3):2619-2642.

[21] Oberlin A BJ, Villey MJKIomfsrP, Editions Technip. Electron microscopic study of kerogen microtexture. Selected criteria for determining the evolution path and evolution stage of kerogen. Kerogen; insoluble organic matter from sedimentary rocks. Paris, France (FRA): Ed. Technip, 1980.; 1980.

[22] Huang L, Zhang L, Shao Q, et al. Simulations of Binary Mixture Adsorption of Carbon Dioxide and Methane in Carbon Nanotubes: Temperature, Pressure, and Pore Size Effects. *The Journal of Physical Chemistry C.* 2007;111(32):11912-11920.

[23] Wu H, Chen J, Liu H. Molecular Dynamics Simulations about Adsorption and Displacement of Methane in Carbon Nanochannels. *The Journal of Physical Chemistry C.* 2015;119(24):13652-13657.

[24] Kumar KV, Müller EA, Rodríguez-Reinoso F. Effect of Pore Morphology on the Adsorption of Methane/Hydrogen Mixtures on Carbon Micropores. *The Journal of Physical Chemistry C.* 2012;116(21):11820-11829.

[25] Changtao Y, Shuyuan L, Hailong W, Fei Y, Xu x. Pore structure characteristics and methane adsorption and desorption properties of marine shale in Sichuan Province, China. *RSC Advances.* 2018;8(12):6436-6443.

[26] Duan S, Gu M, Du X, Xian X. Adsorption Equilibrium

of CO2 and CH4 and Their Mixture on Sichuan Basin Shale. *Energy & Fuels.* 2016;30(3):2248-2256.

[27] Yu S, Bo J, Wu L. Molecular simulation of CH4/CO2/H2O competitive adsorption on low rank coal vitrinite. *Physical Chemistry Chemical Physics.* 2017;19(27):17773-17788.

[28] Yu S, Yan-ming Z, Wu L. Macromolecule simulation and CH4 adsorption mechanism of coal vitrinite. *Applied Surface Science.* 2017;396:291-302.

[29] Zhao T, Li X, Ning Z, Zhao H, Li M. Molecular simulation of methane adsorption on type II kerogen with the impact of water content. *Journal of Petroleum Science and Engineering.* 2018;161:302-310.

[30] Li J, Wang Y, Chen Z, Rahman SS. Insights into the Molecular Competitive Adsorption Mechanism of CH4/CO2 in a Kerogen Matrix in the Presence of Moisture, Salinity, and Ethane. *Langmuir.* 2021;37(43):12732-12745.

[31] Huang L, Ning Z, Wang Q, et al. Effect of organic type and moisture on CO2/CH4 competitive adsorption in kerogen with implications for CO2 sequestration and enhanced CH4 recovery. *Applied Energy.* 2018;210:28-43.

[32] Huang L, Ning Z, Wang Q, et al. Enhanced gas recovery by CO2 sequestration in marine shale: a molecular view based on realistic kerogen model. *Arabian Journal of Geosciences.* 2018;11(15):404.

[33] Zhang J, Clennell MB, Dewhurst DN, Liu K. Combined Monte Carlo and molecular dynamics simulation of methane adsorption on dry and moist coal. *Fuel.* 2014;122:186-197.

[34] Zhou J, Mao Q, Luo KH. Effects of Moisture and Salinity on Methane Adsorption in Kerogen: A Molecular Simulation Study. *Energy & Fuels.* 2019;33(6):5368-5376.

[35] Taulis M, Trumm D, Milke M, Nobes D, Manhire D, O'Sullivan A. Characterisation of coal seam gas waters in New Zealand. *Realising New Zealand's Mineral Potential-Proceedings of the 2005 New Zealand Minerals Conference.* 2005.

[36] Ibrahim A, Nasr-Eldin H. *Effects of Water Salinity, CO Solubility, and Gas Composition on Coal Wettability.* 2015.

[37] Ibrahim AF, Nasr-El-Din HA. Effects of Formation-Water Salinity, Formation Pressure, Gas Composition, and Gas-Flow Rate on Carbon Dioxide Sequestration in Coal Formations. *SPE-87338-PA.* 2017;22(05):1530-1541.

[38] Li J, Wang Y, Chen Z, Rahman SS. Effects of moisture, salinity and ethane on the competitive adsorption mechanisms of CH4/CO2 with applications to coalbed reservoirs: A molecular simulation study. *Journal of Natural Gas Science and Engineering.* 2021;95:104151.

[39] Zhou J, Jin Z, Luo KH. The role of brine in gas adsorption and dissolution in kerogen nanopores for enhanced gas recovery and CO2 sequestration. *Chemical Engineering Journal.* 2020;399:125704.

[40] Dai J, Qin S, Hu G, et al. Major progress in the natural gas exploration and development in the past seven decades in China. *Petroleum Exploration and Development.* 2019;46(6):1100-1110.

[41] Zhang B, Kang J, Kang T. Monte Carlo simulations of methane adsorption on kaolinite as a function of pore size. *Journal of Natural Gas Science and Engineering.* 2018;49:410-416.

[42] Xiong J, Liu X, Liang L, Zeng Q. Adsorption Behavior of Methane on Kaolinite. *Industrial & Engineering Chemistry Research.* 2017;56(21):6229-6238.

[43] Jin Z, Firoozabadi A. Methane and carbon dioxide adsorption in clay-like slit pores by Monte Carlo simulations. *Fluid Phase Equilibria.* 2013;360:456-465.

[44] Chen G, Zhang J, Lu S, et al. Adsorption Behavior of Hydrocarbon on Illite. *Energy & Fuels.* 2016;30(11):9114-9121.

[45] Jin Z, Firoozabadi A. Effect of water on methane and carbon dioxide sorption in clay minerals by Monte Carlo simulations. *Fluid Phase Equilibria.* 2014;382:10-20.

[46] Loganathan N, Bowers GM, Ngouana Wakou BF, Kalinichev AG, Kirkpatrick RJ, Yazaydin AO. Understanding methane/carbon dioxide partitioning in clay nano- and meso-pores with constant reservoir composition molecular dynamics modeling. *Physical Chemistry Chemical Physics.* 2019;21(13):6917-6924.

[47] Tesson S, Firoozabadi A. Deformation and Swelling of Kerogen Matrix in Light Hydrocarbons and Carbon Dioxide. *The Journal of Physical Chemistry C.* 2019;123(48):29173-29183.

[48] Heller R, Zoback M. Adsorption of methane and carbon dioxide on gas shale and pure mineral samples. *Journal of Unconventional Oil and Gas Resources.* 2014;8:14-24.

[49] Jorgensen WL, Maxwell DS, Tirado-Rives J.

Development and Testing of the OPLS All-Atom Force Field on Conformational Energetics and Properties of Organic Liquids. *Journal of the American Chemical Society.* 1996;118(45):11225-11236.

[50] Jorgensen, William, L., Maxwell, David, S. Development and testing of the OPLS all-atom force field on conformational energetics and Properties of Organic Liquids. *Journal of the American Chemical Society.* 1996;118(45):11225-11236.

[51] Srivastava A, Alleman C, Ghosh S, Lee LJ. Molecular dynamics simulation based evaluation of glass transition temperatures of polystyrene in the presence of carbon dioxide. *Modelling and Simulation in Materials Science and Engineering.* 2010;18(6):065003.

[52] Trinh TT, Vlugt TJH, Kjelstrup S. Thermal conductivity of carbon dioxide from non-equilibrium molecular dynamics: A systematic study of several common force fields. *The Journal of Chemical Physics.* 2014;141(13):134504.

[53] Mark P, Nilsson L. Structure and Dynamics of the TIP3P, SPC, and SPC/E Water Models at 298 K. *The Journal of Physical Chemistry A.* 2001;105(43):9954-9960.

[54] Liao Y-T, Manson AC, DeLyser MR, Noid WG, Cremer PS. Trimethylamine N-oxide stabilizes proteins via a distinct mechanism compared with betaine and glycine. *Proceedings of the National Academy of Sciences.* 2017;114(10):2479-2484.

[55] Berendsen HJC, Grigera JR, Straatsma TP. The missing term in effective pair potentials. *The Journal of Physical Chemistry.* 1987;91(24):6269-6271.

[56] Cygan RT, Liang J-J, Kalinichev AG. Molecular Models of Hydroxide, Oxyhydroxide, and Clay Phases and the Development of a General Force Field. *The Journal of Physical Chemistry B.* 2004;108(4):1255-1266.

[57] Jiang, Hao, Economou, Ioannis G, Panagiotopoulos, Athanassios Z. Molecular Modeling of Thermodynamic and Transport Properties for CO2 and Aqueous Brines. *Accounts of Chemical Research.* 2017.

[58] Hou D, Zhang P, Ding Q. Molecular structure and dynamics of aqueous sodium chloride solution in nano-pore between portlandite surfaces: a molecular dynamics study. *Phys Chem Chem Phys.* 2015;18.

[59] Plimpton S. Fast Parallel Algorithms for Short-Range Molecular Dynamics. *Journal of Computational Physics.* 1995;117(1):1-19.

[60] Xiang J, Zeng F, Liang H, Li B, Song X. Molecular simulation of the CH4/CO2/H2O adsorption onto the molecular structure of coal. *Science China Earth Sciences.* 2014;57(8):1749-1759.

[61] Dong K, Zeng F, Jia J, Chen C, Gong Z. Molecular simulation of the preferential adsorption of CH4 and CO2 in middle-rank coal. *Molecular Simulation.* 2019;45(1):15-25.

[62] Mayo SL, Olafson BD, Goddard WA. DREIDING: a generic force field for molecular simulations. *The Journal of Physical Chemistry.* 1990;94(26):8897-8909.

[63] Okiongbo KS, Aplin AC, Larter SR. Changes in Type II Kerogen Density as a Function of Maturity: Evidence from the Kimmeridge Clay Formation. *Energy & Fuels.* 2005;19(6):2495-2499.

[64] Dai B, Hoadley A, Zhang L. Characteristics of high temperature C-CO2 gasification reactivity of Victorian brown coal char and its blends with high ash fusion temperature bituminous coal. *Fuel.* 2017;202:352-365.

[65] Huang L, Ning Z, Wang Q, et al. Molecular simulation of adsorption behaviors of methane, carbon dioxide and their mixtures on kerogen: Effect of kerogen maturity and moisture content. *Fuel.* 2018;211:159-172.

[66] Sarkisov L, Bueno-Perez R, Sutharson M, Fairen-Jimenez D. Materials Informatics with PoreBlazer v4.0 and the CSD MOF Database. *Chemistry of Materials.* 2020;32(23):9849-9867.

[67] Day S, Duffy G, Sakurovs R, Weir S. Effect of coal properties on CO2 sorption capacity under supercritical conditions. *International Journal of Greenhouse Gas Control.* 2008;2(3):342-352.

[68] Loucks R, Reed R, Ruppel S, And D, Jarvie D. Morphology, Genesis, and Distribution of Nanometer-Scale Pores in Siliceous Mudstones of the Mississippian Barnett Shale. *Journal of Sedimentary Research.* 2009;79:848-861.

[69] Ho TA, Wang Y, Criscenti LJ. Chemo-mechanical coupling in kerogen gas adsorption/desorption. *Physical Chemistry Chemical Physics.* 2018;20(18):12390-12395.

[70] Bhowmik S, Dutta P. Investigation into the Methane Displacement Behavior by Cyclic, Pure Carbon Dioxide Injection in Dry, Powdered, Bituminous Indian Coals. *Energy & Fuels.* 2011;25(6):2730-2740.

[71] Sandoval DR, Yan W, Michelsen ML, Stenby EH. Modeling of Shale Gas Adsorption and Its Influence on Phase Equilibrium. *Industrial & Engineering Chemistry Research.* 2018;57(17):5736-5747.

[72] Sui H, Yao J, Zhang L. Molecular Simulation of Shale Gas Adsorption and Diffusion in Clay Nanopores. *Computation.* 2015;3(4).

[73] Gasparik M, Bertier P, Gensterblum Y, Ghanizadeh A, Krooss BM, Littke R. Geological controls on the methane storage capacity in organic-rich shales. *International Journal of Coal Geology.* 2014;123:34-51.

[74] Yang L, Zhou X, Zhang K, Zeng F, Wang Z. Investigation of dynamical properties of methane in slit-like quartz pores using molecular simulation. *RSC Advances.* 2018;8(59):33798-33816.

[75] Rexer TF, Mathia EJ, Aplin AC, Thomas KM. High-Pressure Methane Adsorption and Characterization of Pores in Posidonia Shales and Isolated Kerogens. *Energy & Fuels.* 2014;28(5):2886-2901.

[76] Zhou J, Jin Z, Luo KH. Effects of Moisture Contents on Shale Gas Recovery and CO_2 Sequestration. *Langmuir.* 2019;35(26):8716-8725.

[77] Lu X, Jin D, Wei S, et al. Competitive adsorption of a binary CO_2–CH_4 mixture in nanoporous carbons: effects of edge-functionalization. *Nanoscale.* 2015;7(3):1002-1012.

[78] Busch A, Gensterblum Y, Krooss BM. Methane and CO_2 sorption and desorption measurements on dry Argonne premium coals: pure components and mixtures. *International Journal of Coal Geology.* 2003;55(2):205-224.